



## ABSTRACT

10 Variability in the monthly-mean flow and storm track in the North Pacific  
11 basin is examined with a focus on the near-surface baroclinicity. Dominant  
12 patterns of anomalous near-surface baroclinicity found from EOF analyses  
13 generally show mixed patterns of shift and changes in the strength of near-  
14 surface baroclinicity. Composited anomalies in the monthly-mean wind at  
15 various pressure levels based on the signals in the EOFs show accompany-  
16 ing anomalies in the mean flow up to 50 hPa in the winter and up to 100  
17 hPa in other seasons. Anomalous eddy fields accompanying the anomalous  
18 near-surface baroclinicity patterns exhibit, broadly speaking, structures antic-  
19 ipated from simple linear theories of baroclinic instability, and suggest a ten-  
20 dency for anomalous wave fluxes to accelerate–decelerate the surface west-  
21 erly accordingly. However, the relationship between anomalous eddy fields  
22 and anomalous near-surface baroclinicity in the midwinter is not consistent  
23 with the simple linear baroclinic instability theories. Composited anomalous  
24 SST accompanying anomalous near-surface baroclinicity often exhibits mod-  
25 erate values and large spatial scales in the basin, rather than large values con-  
26 centrated near the oceanic fronts. In the midsummer and in some cases in  
27 cold months, however, large SST anomalies are found around the Kuroshio–  
28 Oyashio Extensions. Accompanying anomalies in the net surface heat flux,  
29 SST in the preceding and following months, and meridional eddy heat flux  
30 in the lower troposphere suggest active roles played by the ocean in generat-  
31 ing the concomitant anomalous large-scale atmospheric state in some of these  
32 cases.

## 33 1. Introduction

34 It has now become our basic knowledge that the extratropical atmosphere is driven strongly by  
35 the horizontal potential temperature gradient that arises from the differential solar heating (e.g.,  
36 Lorenz 1955). The horizontal gradient in the potential temperature, often referred to as baro-  
37 clinicity, is a measure of upper-level wind steering via thermal wind and a measure of baroclinic  
38 instability in the atmosphere. Baroclinicity in the lower atmosphere in classic theories of atmo-  
39 spheric stability is measured by a combination of the static stability and horizontal temperature  
40 gradient, the latter of which is equivalent to vertical shear in the horizontal wind through the ther-  
41 mal wind balance (Charney 1947; Eady 1949). In its original form, the Eady's maximum growth  
42 rate for baroclinic instability  $B_{GRMax}$  is defined by  $B_{GRMax} = 0.31(|f|/N)(\partial U/\partial z)$  in a zonally  
43 homogeneous steady mean state, where  $U$  is the mean zonal flow,  $f$  is the Coriolis parameter, and  
44  $N$  is the Brunt-Väisälä frequency. Charney's formula is slightly different from the Eady's, but still  
45 incorporates the same effects.

46 Lindzen and Farrell (1980) first applied the Eady's parameter to atmospheric data to successfully  
47 estimate the maximum growth rate of baroclinic instability in the troposphere. Hoskins and Valdes  
48 (1990) used its localized version (i.e.,  $U$ ,  $N$ , and  $f$  are all local Eulerian mean values) as the  
49 central parameter in their study of the Northern Hemispheric storm tracks. This local version, or  
50 its simplified version, has been used successfully as an indicator of baroclinic wave generation in  
51 diagnostic studies of stormtracks in recent years as well (Nakamura and Sampe 2002; Nakamura  
52 and Shimpo 2004; Nakamura et al. 2004). In our study, the North Atlantic part of which was  
53 reported in Nakamura and Yamane (2009, hereafter Part I), we define the near-surface baroclinic  
54 vector,  $\mathbf{B} = B^x\mathbf{i} + B^y\mathbf{j}$ , where  $B^x = -(g/\theta N)(\partial\theta/\partial y)$  and  $B^y = (g/\theta N)(\partial\theta/\partial x)$  with  $\theta$  being the  
55 monthly-mean potential temperature at 2 m above the surface, and use it as the central quantity

56 of the diagnoses. Unless stated otherwise, “anomalies” refer to deviations from the climatology  
57 hereafter. Though its meridional component does not appear in any classic theory of baroclinic  
58 instability, a theory that does incorporate the effect of  $B^y$  shows its important role in enhancing  
59 baroclinic wave generation locally to the east of the mean trough (Niehaus 1980). In the North  
60 Atlantic storm track region, we indeed found that the substantial zonal gradient in the surface  
61 temperature in and around the Labrador Sea plays a major role in the large-scale atmospheric  
62 state.

## 63 **2. The sea surface temperature**

64 The sea surface temperature (SST) is an important factor in determining  $\mathbf{B}$  in the storm-track  
65 regions (e.g., Hoskins and Valdes 1990; Nakamura et al. 2004; Part I). SST anomalies (SSTAs)  
66 around an oceanic front along the Gulf Stream (GS), Kuroshio Extension (KE), or Oyashio Extension  
67 (OE) can have a profound impact on  $\mathbf{B}$  along the storm tracks.

### 68 *a. A subtle point*

69 A subtle but important point that has to be considered carefully in this regard is the spatial  
70 scale and the location of SSTAs with respect to the climatology, since it is the anomalous surface  
71 temperature gradient whose structure has a spatial scale of the atmospheric Rossby deformation  
72 radius that can exert significant influence on the large-scale atmospheric flow.

### 73 1) CHANGES IN THE TEMPERATURE

74 The high sensitivity of  $\mathbf{B}$  to changes in the temperature contrast across the front and changes  
75 in the width of the front, and the uncertainty in the impact of SSTAs of small spatial scales on  
76  $\mathbf{B}$  make it difficult to assess the effective  $\mathbf{B}$  anomalies that are attributable to the SSTAs from the

77 available data. Moreover, it is uncertain exactly how the SSTAs in the presence or absence of the  
78 land surface temperature anomalies may or may not produce **B** anomalies that are significant to  
79 the atmosphere.

80 *(i) Complicating factor* The complicating factor introduced by the land surface must be taken  
81 into account when studying potential roles of extratropical SSTAs in the extratropical atmospheric  
82 anomalies.

83 Lau (1988) investigated patterns of anomalous storm track activity and associated low-frequency  
84 flow anomalies by computing empirical orthogonal functions (EOFs) for high-frequency 500-hPa  
85 geopotential height for the Northern Hemisphere winters. He found that both North Atlantic and  
86 North Pacific storm tracks have a pattern of meridional shift and a pattern of increased or de-  
87 creased eddy activity in the first two EOFs. He also found that these changes in the storm tracks  
88 have symbiotic relationships with the background flows and have substantial impacts on the mean  
89 flow. Part I approached the issue of the stormtrack and low-frequency flow variability in connec-  
90 tion with SSTAs in the extratropics, focusing on **B** as the key parameter of diagnoses, and found  
91 similar patterns of variability in the eddy activity and low-frequency flow in the North Atlantic  
92 basin. Much of this variability was connected to SSTAs in the vicinity of the Gulf Stream in cold  
93 months (Part I). Since the winter North Pacific basin has a storm track and mean flow that appear  
94 to be related to the oceanic fronts, Kuroshio–Oyashio Extensions (KOE) in this case, in a manner  
95 essentially the same as those in the North Atlantic basin related to the GS, we have attempted to  
96 find similar results for the North Pacific basin. In this regard, we have chosen not to project our  
97 results onto the major mode of variability in the extratropical North Pacific basin, the North Pa-  
98 cific decadal variability (PDV), so that our presentation and discussion are mostly confined to the  
99 wave–mean flow dynamics of monthly time scale or shorter.

100 Our approach to the search for a link between anomalies in the KOE and the overlying at-  
101 mosphere is as follows: (i) identify dominant patterns in anomalous  $\mathbf{B}$  in the storm track for each  
102 calendar month and identify years in which the anomaly fits the pattern well, (ii) composite anoma-  
103 lies in the monthly-mean circulation and high-frequency transients in the atmosphere to obtain a  
104 typical atmospheric state that accompanies the patterns of anomalous  $\mathbf{B}$ , (iii) composite SSTA to  
105 obtain a typical oceanic state that accompanies and precedes the patterns of anomalous  $\mathbf{B}$ , and (iv)  
106 composite anomalous net surface heat flux that accompanies and precedes the pattern of anoma-  
107 lous  $\mathbf{B}$ . With this approach, we obtain typical pictures of anomalous states in the atmosphere and  
108 oceans with anomalous  $\mathbf{B}$  as their connecting interface. Section 2 describes the data and procedure  
109 to compute  $\mathbf{B}$ . Section 3 describes the climatology and variance of  $\mathbf{B}$ . Dominant patterns of  $\mathbf{B}$  are  
110 shown in section 4, followed by composited anomalies in various atmospheric fields and SST in  
111 section 5. Finally, we present our discussion on the results, examining a potential cause–effect  
112 relationship between anomalies in the SST and atmosphere in section 6.

113 Figure 1 shows the climatology of  $B_x$ ,  $U^{200}$ ,  $\overline{V'\theta'}^{850}$ ,  $\overline{V'\theta'}^{200}$ ,  $MR^{850}$ ,  $U^{1000}$ , SST, and  $F_h$  for  
114 February and August as examples of the reference state in the winter and summer. The numeric  
115 superscript indicates the pressure level in hPa. The seasonal mean is visibly more diffused in  
116 structure, particularly for  $B_x$ , than those shown in Fig. 1. There are no surprises in the overall  
117 picture of  $B_x$ . The regions of large land–sea temperature contrast and the oceanic fronts show very  
118 large  $B_x$  in cold months. The position of  $B_x$  maximum in the storm track region is found along  
119 the KOE region throughout the year. The zonally elongated band of large  $B_x$  in the storm track is  
120 generally wider in cold months than in warm months. In fact, large  $B_x$  values that presumably  
121 accompany the Kuroshio and its extension in the cold months vanish in the summer (Figs. 1a,b).  
122 The seasonal variation in the  $B_x$  values in the storm track basically follows that of the north–south  
123 differential heating—largest in the winter and smallest in the summer. As reported by Nakamura

124 et al. (2004), the  $U^{200}$  maximum is displaced southward from the Bx maximum visibly in winter  
125 months (Fig. 1a), although U200 is generally large over the area of large Bx in the core of the storm  
126 track. The southward displacement of the U200 maximum from the Bx maximum in the storm  
127 track is less pronounced or even reversed in warmer months (Fig. 1b). We note that the structure  
128 of the climatological Bx generally reflects those of  $(\partial\theta^{2m}/\partial y)$  with some exceptions where the  
129 surface slope contributes significantly to Bx in isolated areas over the land, most notably around  
130 the Himalayas.

131 The position and structure of the storm track as indicated by  $\overline{V'\theta'}^{850}$  and  $\overline{V'V'}^{200}$  are, at least for  
132 the winter, essentially the same as those reported in earlier studies on the storm tracks (e.g., Chang  
133 et al. 2002). The maxima in  $\overline{V'\theta'}^{850}$  and  $\overline{V'V'}^{200}$  are located in the band of large Bx.

### 134 3. Data and calculation procedures

135 The data used to calculate  $\mathbf{B}$  are the monthly-mean temperature at 2 m above the surface ( $T^{2m}$ )  
136 and temperature at pressure levels available from the 40-yr European Centre for Medium-Range  
137 Weather Forecasts (ECMWF) Re-Analysis (ERA-40; Uppala et al. 2005). We chose the ERA-40  
138  $T^{2m}$  data rather than the National Centers for Environmental Prediction–National Center for At-  
139 mospheric Research (NCEP–NCAR) reanalysis products for its explicit inclusion of the observed  
140 near-surface temperature in producing the  $T^{2m}$  data. The monthly-mean surface pressure data  
141 from the NCEP–NCAR reanalyses (Kalnay et al. 1996) were used to determine the pressure levels  
142 to be used for  $\mathbf{B}$  calculation, and to calculate  $\theta$  at 2 m above the surface from  $T^{2m}$ . We used the  
143 NCEP–NCAR surface pressure data for convenience, since we had already compiled the dataset  
144 for calculating transient eddy fluxes to be mentioned later and the ERA-40 surface pressure data  
145 are not readily available. We later compared the NCEP–NCAR monthly-mean sea level pressure  
146 with that of ERA-40, and found the difference between the two products to be immaterial for the

147 purpose of the current study. We also used ERA-40 monthly-mean horizontal wind and geopo-  
148 tential height at pressure levels, net surface heat flux,  $F_h$  (the sum of latent heat flux, sensible  
149 heat flux, solar radiation, and the thermal radiation), and Hadley Centre sea surface temperature  
150 data (Rayner et al. 2003) to compile anomaly composites accompanying anomalous patterns in  
151 **B**. In addition, we used 6-hourly temperature and wind data from the NCEP–NCAR reanalyses to  
152 compute various eddy fields. The accuracy of the  $F_h$  data used here is, as true for other reanalyses  
153 surface heat flux products, may not be so high to produce reliable anomaly composites.

154 We computed **B** near the surface by calculating the horizontal gradient in  $\theta^{2m}$ , using the centered  
155 finite differencing, and calculating  $N$  from the lowest three vertical pressure levels that are location  
156 dependent because of topography. Both  $\nabla\theta^{2m}$  and  $N$  were calculated locally as in Hoskins and  
157 Valdes (1990) and Nakamura and Shimpo (2004). The entire 45 yr from September 1957 to August  
158 2002 were used for the Northern Hemisphere. To resolve the dominant modes in **B** arising from  
159 the land–sea temperature contrast, one may need much higher horizontal resolution in the data.  
160 The relatively coarse horizontal resolution of the data may artificially suppress the significance of  
161 the variability associated with the land–sea temperature contrast. One should keep this limitation in  
162 mind. The 6-hourly bandpassed (period of 2–7 days) eddy fields and ultra-low-frequency (period  
163 of 30 days and longer) background fields were computed from the NCEP– NCAR reanalyses,  
164 using simple time filters (Lau and Lau 1984) first. The filtered time series were then visually  
165 examined against the raw time series and, then, used to calculate the slowly evolving bandpassed  
166 meridional velocity variance ( $\overline{V'V'}$ ), meridional temperature flux ( $\overline{V'\theta'}$ ), and the three-dimensional  
167 transient wave activity flux defined on a zonally varying basic state by Plumb (1986). The wave  
168 activity flux consists of the zonal and meridional advective fluxes (MU and MV), the zonal and  
169 meridional radiative fluxes (MRx and MRy), and the radiative vertical flux (MRz). The flux is  
170 essentially the Eliassen–Palm flux (Eliassen and Palm 1961) in a zonally inhomogeneous mean



171 flow (Plumb 1986). The wave activity flux was calculated from February 1948 to November 2004  
 172 only for the extratropics poleward of 20° latitude. Also, it was calculated only from 850 to 30 hPa  
 173 because of the double differentiation with respect to pressure required for the calculation. The flux  
 174 of particular interest in this study is the vertical component. Here  $MR^z$  is defined by

$$MR^z = \frac{pf \cos \phi}{p^0 |\nabla h \bar{q}| (d\theta_0/dz)} \left( \frac{\partial \bar{q}}{\partial x} \overline{U' \theta'} + \frac{\partial \bar{q}}{\partial y} \overline{V' \theta'} \right),$$

175 where  $q$  is quasigeostrophic potential vorticity,  $p$  is the pressure,  $p^0$  is the reference surface pres-  
 176 sure set to 1000 hPa here,  $\theta_0$  is the area-weighted ultra-low-frequency hemispheric mean potential  
 177 temperature at each height,  $u_9$  is the bandpassed potential temperature, and  $z$  is the geopotential  
 178 height. An overbar denotes an ultra-low frequency component and a prime denotes bandpassed  
 179 component. The 6-hourly time series of wave fluxes was computed by using the time series of  
 180 ultra-low-frequency fields as the basic-state and high-frequency fields as eddies. In short, the time  
 181 series was calculated by changing the meaning of an overbar from the time mean state to an ultra-  
 182 low-frequency state, and changing the meaning of a prime from a departure from the mean to a  
 183 high-frequency state. The 6-hourly eddy time series was averaged over each month to produce  
 184 monthly-mean time series. This dataset allows us to examine anomalous eddy fields accompany-  
 185 ing anomalous  $\mathbf{B}$  in specific months. The climatology for the eddy fields was computed from 46  
 186 yr, January 1958 to December 2003. The calculation of the wave activity and its flux is described  
 187 in detail by Nakamura et al. (2010).

#### 188 4. Climatology and variance

189 The climatology and variance of  $B_x$  and  $B_y$  were computed for each calendar month and exam-  
 190 ined closely for their spatial and temporal structures. The monthly climatology, rather than the  
 191 seasonal climatology, is used as the reference in our study, to avoid contamination of the diagnos-

192 tic results arising from differences in the climatology between two successive months. Unlike in  
193 the North Atlantic basin reported in Part I, we found the impact of  $B_y$  variations on the large-scale  
194 atmospheric state in the North Pacific basin much weaker than that of  $B_x$  variations, presumably  
195 because of the more zonal orientation of the KOE in comparison to the Gulf Stream and North At-  
196 lantic Current. In the following, thus, we focus our presentation on the climatology and variations  
197 of  $B_x$  and their impact on the large-scale atmospheric state.

198 Sample citations: ?, ?, and (???)

199 *Acknowledgments.* We thank two anonymous reviewers for their comments, which helped to  
200 improve the manuscript.

201 APPENDIX

202 **Appendix Title**

203 *Appendix section head*

204 Here is a sample appendix.

$$\frac{pf \cos \phi}{p^0 |\nabla h \bar{q}| (d\theta_0/dz)} \tag{A1}$$

205 APPENDIX B

206 **Second Appendix Title**

207 *a. Sample appendix section head*

208 Second appendix example.

209 *b. Sample appendix section head*

$$\left( \frac{\partial \bar{q}}{\partial x} U' \theta' + \frac{\partial \bar{q}}{\partial y} V' \theta' \right) \quad (\text{B1})$$

210 **LIST OF TABLES**

211 **Table 1.** Percentage of variance explained by the first four EOFs for the North Pacific  
212 Bx. The degree of separation between EOF1 and EOF2 and EOF2 and EOF3,  
213 based on the North et al. (1982) criterion, is indicated by good (GD) and not  
214 good or marginal (NG). . . . . 13

215 **Table 2.** Years selected for anomaly composites for the positive phase of  $B^x$  EOF1. . . . . 14

216 **Table 3.** Years selected for anomaly composites for the negative phase of  $B^x$  EOF1. . . . . 15

217 TABLE 1. Percentage of variance explained by the first four EOFs for the North Pacific Bx. The degree of  
 218 separation between EOF1 and EOF2 and EOF2 and EOF3, based on the North et al. (1982) criterion, is indicated  
 219 by good (GD) and not good or marginal (NG).

Month	EOF1	Split	EOF2	Split	EOF3	EOF4
Jan	29	NG	24	GD	10	5
Feb	39	GD	20	GD	7	6
Mar	31	GD	14	NG	10	6
Apr	23	GD	14	NG	10	7
May	19	GD	12	NG	10	7
Jun	19	GD	12	NG	10	9
Jul	18	NG	13	NG	9	7
Aug	18	NG	13	NG	11	9
Sep	17	NG	13	NG	10	8
Oct	16	NG	13	GD	8	7
Nov	19	NG	16	NG	11	8
Dec	33	GD	18	GD	10	6

TABLE 2. Years selected for anomaly composites for the positive phase of  $B^x$  EOF1.

Month	Yr of positive phase
Jan	1961, 1969, 1978, 1979, 1988, 1990, 1992, 1994
Feb	1964, 1977, 1978, 1980, 1983, 1986, 1988, 2000, 2001
Mar	1970, 1973, 1979, 1980, 1984, 1988, 2000
Apr	1959, 1961, 1962, 1963, 1968, 1972, 1983, 2002
May	1971, 1984, 1993, 1996, 2000
Jun	1981, 1983, 1984, 1993, 1998
Jul	1961, 1972, 1973, 1978, 1994, 2000
Aug	1967, 1970, 1973, 1978, 1994, 1999
Sep	1975, 1977, 1988, 1989, 1994, 1998, 1999
Oct	1962, 1977, 1998, 1999, 2001
Nov	1985, 1986, 1987, 1988, 1991, 1998
Dec	1957, 1968, 1972, 1978, 1979, 1990

TABLE 3. Years selected for anomaly composites for the negative phase of  $B^x$  EOF1.

Month	Yr of negative phase
Jan	1962, 1963, 1968, 1974, 1991, 1996, 1997
Feb	1959, 1963, 1971, 1974, 1976, 1979, 1985, 1989, 1990, 1994
Mar	1963, 1968, 1972
Apr	1984, 1988, 1993, 1996, 1999, 2000
May	1961, 1963, 1983, 1987, 1997
Jun	1961, 1972, 1978, 1980, 1982, 1986
Jul	1964, 1974, 1980, 1983, 1986, 1988, 1993
Aug	1980, 1987, 1991, 1993, 1997
Sep	1959, 1963, 1969, 1983, 1985, 1993
Oct	1957, 1986, 1993, 1996, 1997
Nov	1958, 1968, 1970, 1982, 1997
Dec	1969, 1974, 1976, 1985, 1998, 1999, 2000, 2001

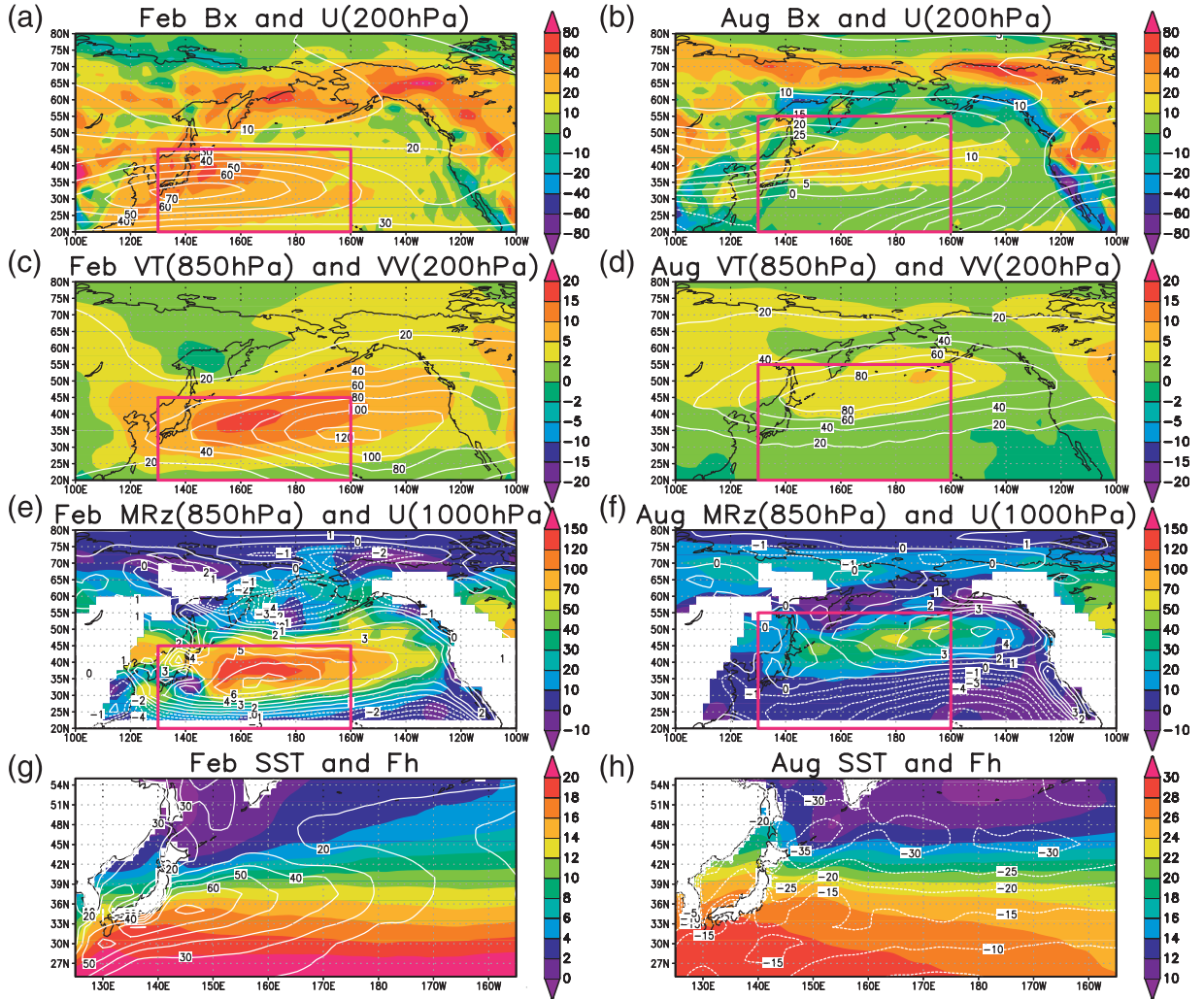
220 **LIST OF FIGURES**

221 **Fig. 1.** Climatology of  $Bx(10^{-6}s^{-1}$ , color) and  $U^{200}(m s^{-1}$ , contours) for (a) February and (b)  
 222 August;  $\overline{V'\theta'}^{850}$  (K m s<sup>-1</sup>, color) and  $\overline{V'V'}^{200}$  (m<sup>2</sup> s<sup>-1</sup>, contours) for (c) February and (d)  
 223 August;  $MR^{z850}$  ( $10^{-3} m^2 s^{-2}$ , color) and  $U^{1000}$  (m s<sup>-1</sup>, contours) for (e) February and (f)  
 224 August; and SST (K, color) and  $F_h [10^5 J m^{-2} (6 h)^{-1}]$  for (g) February and (h) August.  
 225 Red rectangles indicate the domain of EOF calculations. . . . . 17

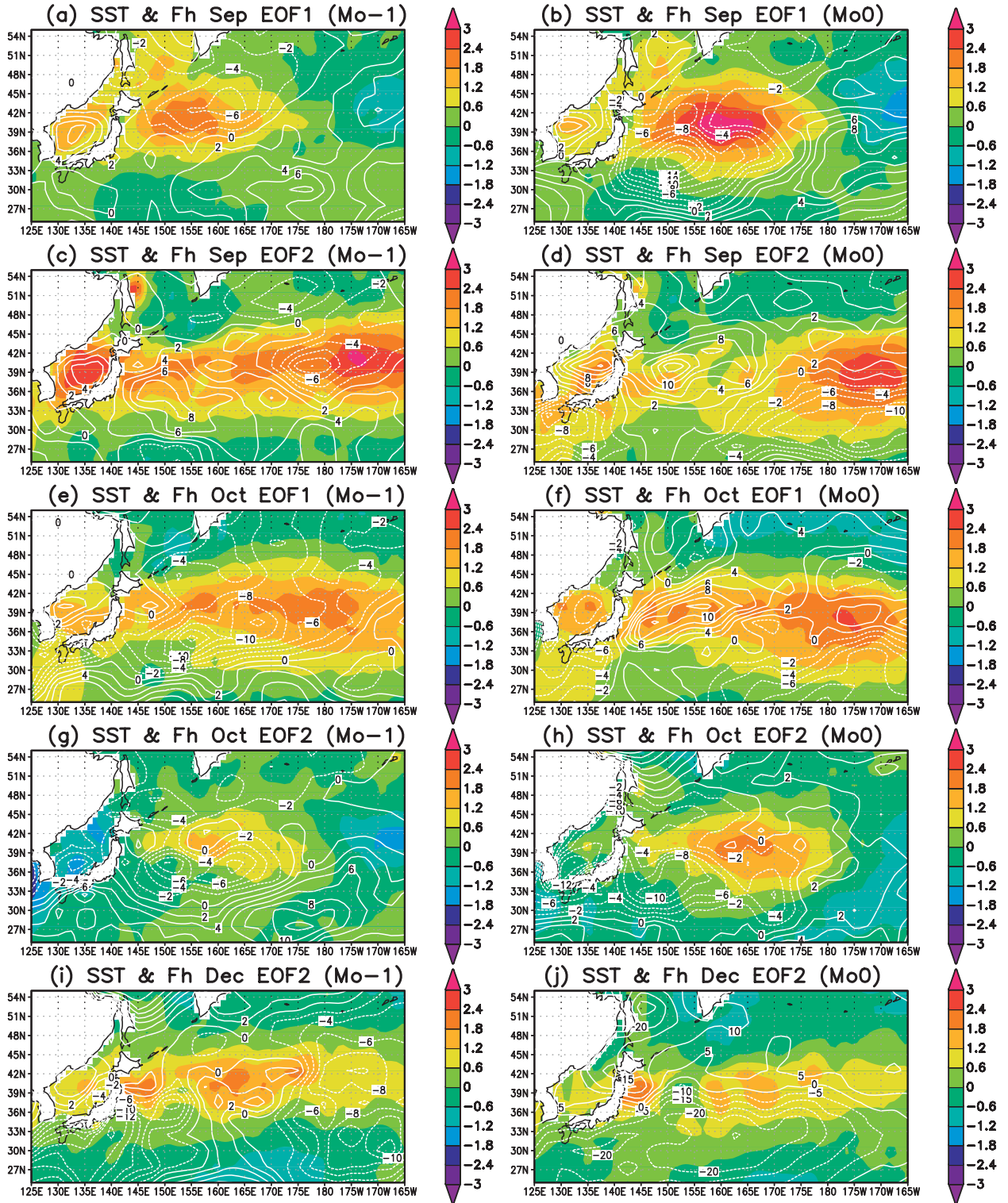
226 **Fig. 2.** As in Fig. 10, but for (a),(b) September EOF1; (c),(d) September EOF2; (e),(f) October  
 227 EOF1; (g),(h) October EOF2; and (i),(j) December EOF2. . . . . 18

228 **Fig. A1.** Here is an appendix, single column figure caption. . . . . 19





229 FIG. 1. Climatology of  $Bx(10^{-6}s^{-1}$ , color) and  $U^{200}(m s^{-1}$ , contours) for (a) February and (b) August;  
 230  $\overline{V'\theta}^{850}$  ( $K m s^{-1}$ , color) and  $\overline{V'V'}^{200}$  ( $m^2 s^{-1}$ , contours) for (c) February and (d) August;  $MRz^{850}$  ( $10^{-3} m^2$   
 231  $s^{-2}$ , color) and  $U^{1000}$  ( $m s^{-1}$ , contours) for (e) February and (f) August; and SST ( $K$ , color) and  $F_h$  [ $10^5 J m^{-2}$   
 232 ( $6 h$ ) $^{-1}$ ] for (g) February and (h) August. Red rectangles indicate the domain of EOF calculations.



233 FIG. 2. As in Fig. 10, but for (a),(b) September EOF1; (c),(d) September EOF2; (e),(f) October EOF1; (g),(h)  
 234 October EOF2; and (i),(j) December EOF2.

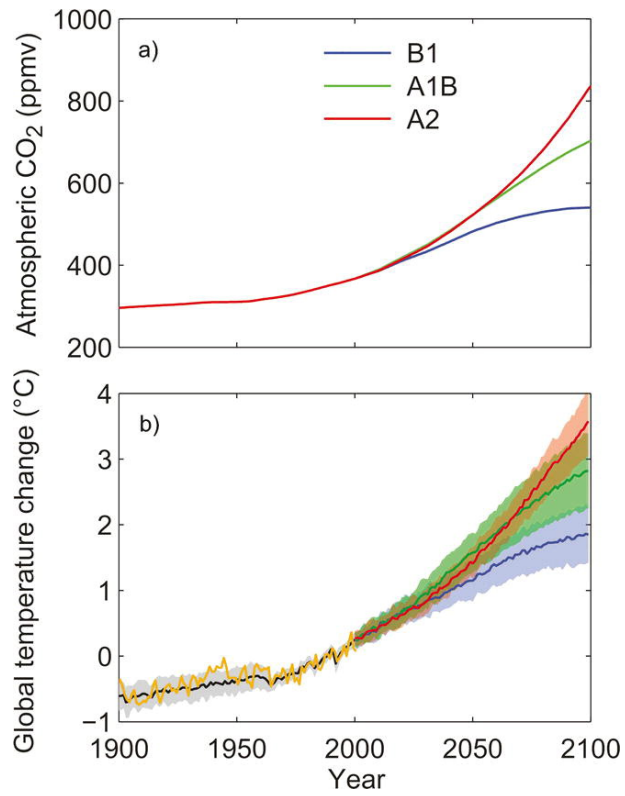


Fig. A1. Here is an appendix, single column figure caption.